10.2514/6.2015-0174

AIAA SciTech Forum
5-9 January 2015, Kissimmee, Florida
56th AIAA/ASCE/AHS/ASC Structures, Structural Dynamics, and Materials Conference

Forced and Aeroelastic Response of Bird-Damaged Fan Blades – A Comparison and Its Implications

Eric R. Muir* and Peretz P. Friedmann†

Department of Aerospace Engineering, The University of Michigan, Ann Arbor, MI, 48109, USA

The aeroelastic response of a bird-damaged fan stage at the inlet of a high-bypass ratio turbofan engine is examined using a combined computational fluid dynamics and computational structural dynamics framework. The damaged fan sector consists of 5 blades obtained from accurate numerical simulation of the bird impact. Forced and aeroelastic response calculations are performed and compared to assess the role of aeroelastic coupling. The calculations are performed at 100%, 75%, and 60% throttle setting to investigate the role of engine speed on the fan response. Results from the forced response and aeroelastic response calculation indicate that the undamaged blades opposite the damaged sector exhibit the highest level of structural response. Comparing the forced response with the aeroelastic response shows increased particiation of the higher structural modes, especially for the damaged blades, that grow in time or exhibit beating. Examination of the work performed by the aerodynamic forces suggests that the growth in blade response is due to aeroelastic phenomena and can cause a potential instability. The results illustrate the importance of aeroelastic effects when predicting the post bird strike fan response.

Nomenclature

$\dot{m}$	Mass flow rate
$\dot{m}_R$	Referred mass flow rate
q_m	Generalized degree of freedom of the m^{th} mode
P	Aerodynamic total pressure
PR	Total pressure ratio
t	Time
T	Aerodynamic total temperature
W_{AR}	Aerodynamic work from aeroelastic calculations
W_{FR}	Aerodynamic work from forced response calculations
$\mathbf{F}_{\text{aero}}$	Assembled aerodynamic force vector
$\mathbf{F}_{\Omega}$	Assembled centrifugal force vector
$\mathbf{K}$	Global structural stiffness matrix
$\mathbf{M}$	Global structural mass matrix
$\mathbf{U}$	Assembled nodal deformation vector
$\mathbf{x} = \{x, y, z\}^T$	Nodal position vector

Coordinate Systems

$< r, \theta, z >$	Global cylindrical coordinate system
$< x, y, z >$	Global Cartesian coordinate system

*Post Doctoral Research Fellow, Member AIAA
†François-Xavier-Xavier Bagnound Professor of Aerospace Engineering, Fellow AIAA and AHS

Greek Symbols

$\mathbf{\Phi}_m$	Mode shape deformation of the m^{th} mode

Subscripts

m	Mode number
STD	Standard atmosphere conditions

Superscripts

$\dot{(\ )}=d/dt$	Differentiation with time

Abbreviations

1B	First bending mode
1T	First torsion mode
2B	Second bending mode
2T	Second torsion mode
3B	Third bending mode
CFD	Computational Fluid Dynamics
CSD	Computational Structural Dynamics
FAA	Federal Aviation Administration
FAR	Federal Aviation Regulation
FE	Finite element
FEM	Finite element method
FSI	Fluid structure interface
RANS	Reynolds-averaged Navier-Stokes

I. Introduction, Background, and Objectives

Bird strike on jet engine fan blades is important for the design of both civilian and military aircraft. Bird strikes occur primarily during takeoff and landing due to the tendency of birds to congregate in the vicinity of the ground.[1] The low altitude at which bird strikes occur limits recovery options and enhances the risk due to bird strike. The turbofan engines used in commercial and military aircraft have a large intake area covered by fan blades that increases the chance of bird strikes. During bird-strike, the bird hits the fan blades, fragments, and propagates through the engine core and bypass duct. The impact can cause substantial deformation of the blade leading edge over a large region of the blade span accompanied by global bending and twist of the blade.[2] Furthermore, the thin, low aspect ratio, low camber fan blades used in modern turbofans are structurally and aerodynamically optimized for efficiency at normal operating conditions, and bird damage induces off-design operation.[3]

The Federal Aviation Administration (FAA) mandates comprehensive standards for bird strike resistance.[4–6] Engine certification requires successful demonstration of compliance with Federal Aviation Regulation (FAR) Part 33 in which a bird is fired with an air cannon at a test stand mounted, running engine.[6] The damaged engine must maintain 75% of the maximum rated thrust and meet engine handling requirements for a series of post bird strike operating conditions that simulate an emergency landing sequence. Figure 1 provides a throttle "skyline" chart that describes the sequence of throttle settings for the run-on demonstration.

Assuming the fan blades withstand the initial impact, the run-on demonstration is particularly challenging. Aerodynamic disturbances caused by the bird damage, such as flow separation, vortex shedding, and shock oscillations, can result in sustained thrust loss. Furthermore, these aerodynamic disturbances also introduce significant unsteady aerodynamic forces that can couple with the structural dynamics to produce a complex aeroelastic response problem that can lead to aeroelastic instability.[7,8] Therefore, predicting the aeroelastic behavior of a bird-damaged fan blade represents a significant design barrier in the development of improved-efficiency turbofan engines.[1]

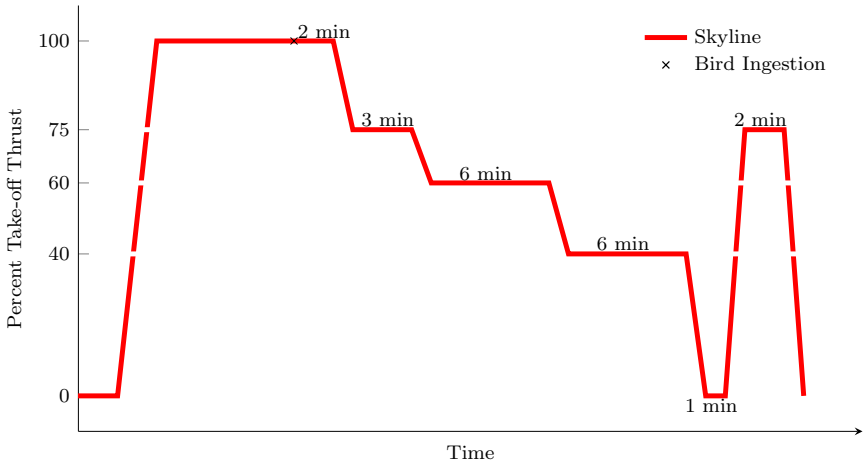

Figure 1. Throttle "skyline" chart for run-on demonstration.

Numerical simulations provide a cost effective means for assessing the aerodynamic loading and aeroelastic behavior of a damaged fan. However, the combined aerodynamic and structural dynamic modeling of a bird-damaged fan assembly, where the damage is typically isolated to a sector of blades, is a complex problem. Computational structural dynamics (CSD) based on the finite element method (FEM) are typically used to model the bird impact and resulting structural response since it can represent complex material behavior and nonlinear geometric deformations.[9–15] Computational fluid dynamics (CFD) is required to accurately capture the complex flow phenomena associated with bird damaged turbofans.[16–19] Reliable CSD and CFD methods exist to compute the bird impact, structural dynamic response, and unsteady aerodynamic loads of a damaged fan blade. However, due to the computational times required for CFD methods, the structural and aerodynamic computations are typically performed separately in an uncoupled manner. Therefore, the aeroelastic effects that may be important in the bird strike problem are not properly accounted for.

Two primary methods are used to couple the CSD and CFD components: the "classical approach which ignores the interaction between the fluid and structure and the integrated approach which attempts to account for it. Forced response calculations utilize a "classical" or one-way coupled approach to calculate the effect of the unsteady flow field on the structural response.[19–21] In this approach, the aerodynamic calculations are performed first for a rigid geometry. Subsequently, the unsteady aerodynamic forces are extracted and applied on the structural dynamic model of the blade. The aerodynamic model is not affected by the structural response, thus the feedback mechanism of the structural response on the unsteady aerodynamic loading is not captured. In contrast, aeroelastic response calculations are performed using an integrated or two-way coupled approach that combines the aerodynamic and structural dynamic models and fully captures the combine aeroelastic behavior.[19–22]

Despite its importance, only a limited number of computational studies have considered the aerodynamic behavior and aeroelastic response of a bird-damaged fan. Bohari and Sayma[23] presented a CFD approach for analyzing the aerodynamic characteristics of a bird-damaged NASA rotor 67 containing a single blade with "assumed" leading edge damage. The steady-state CFD results conclude that the stall margins deteriorate for the damaged fan with stall occurring below the design operating line. Imregun et al.[16,17] conducted two unique studies that examine the aeroelastic response and stability of a bird-damaged bladed disk containing two damaged blades using a fully coupled CSD/CFD formulation to determine the time-dependent response. In Ref. 16, the fully coupled analysis demonstrates instability of the first torsion mode of a damaged blade; however, it is unclear if the growth in modal displacement is the result of a flutter mechanism or the strong wake shed by the upstream damaged blade. These findings are inconclusive since the fully-coupled calculations were only performed for 1/3 fan revolution due limitations on the available computer resources. In a follow-up study, Ref. 17, the aeroelastic stability was also found to be sensitive to flight conditions with flutter margins reduced at low pressure ratios and rotating stall occurring at high pressure ratios.

These studies provide insight into the aerodynamic behavior and aeroelastic response of a bird-damaged fan. However, the damage sector was limited to one or two blades, and the form of the damage did not resemble a configuration resulting from bird-strike certification tests. Furthermore, the aeroelastic response

calculations of Refs. 17 and 16 were performed at 70% engine rotational speed, and the aeroelastic behavior of the damaged fan at other engine speeds was not considered. Therefore, it is evident that a computational aeroelastic study of a bird damaged commercial turbofan, with damage representative of experimental bird strike tests or accurate numerical simulation of the bird strike event, is required to improve our fundamental understanding of the bird-strike problem.

In Ref. 24, the authors presented an aerodynamic model that is capable of capturing the behavior of a damaged fan sector of a commercial turbofan engine and is suitable for modeling both the forced and aeroelastic response of the bird damaged blades. Subsequently in Ref. 25, the aerodynamic model and a structural dynamic model were combined to produce the forced response behavior so as to gain insight into this complex system. In Ref. 26, the forced response framework was extended to accommodate two-way coupling between the aerodynamic and structural dynamic models of the bird damaged fan and preliminary aeroelastic response calculations were performed. In this paper, the combined CFD and CSD framework is implemented to compare the blade response resulting from one-way forced response and fully-coupled aeroelastic response calculations and thus assess the role of complete aeroelastic coupling on the response. The calculations were performed at the 100%, 75%, and 60% throttle settings on the skyline chart in Fig. 1 to examine the effect of engine speed on the fan response. The specific objectives of the current study are:

1. Present a coupled CFD/CSD framework for one-way forced response and fully-coupled aeroelastic response calculations of a bird damaged fan.

2. Study in detail the forced and aeroelastic response of a bird-damaged fan stage under post bird strike conditions at 100%, 75%, and 60% throttle settings.

3. Compare the blade response resulting from one-way forced response and fully-coupled aeroelastic response calculations to assess the role of complete aeroelastic coupling on the response.

4. Compare the aerodynamic work calculated from the forced and aeroelastic response calculations so as to identify the potential for aeroelastic instability.

II. Damaged Fan Configuration

The turbofan geometry examined is representative of a commercial, high-bypass ratio turbofan. LS-DYNA is employed to numerically simulate the bird strike problem and obtain the bird-damaged configuration. The LS-DYNA code has been extensively used to model bird strike problems and has proven itself a reliable tool for computing the damaged blade configurations.[9,15] The damaged geometry considered is due to a single 2.5 pound (lb) bird ingested at take-off conditions at a strike location of 70% blade span. The bird strike calculation is restricted to a sector consisting of a subset of 5 blades cantilevered at the root, and the remaining blades are undamaged. The fan material is modeled as an elasto-plastic material with a piecewise linear stress-strain relationship where the yield stress is dependent on the strain rate. The bird model is assumed to be an ellipsoid, and a viscous material model is employed to capture the impact properties. Figure 2 shows the damaged fan configuration, where the damaged blades are highlighted in orange and the blades are numbered.

III. Aerodynamic Model

The ANSYS CFX commercial aerodynamic solver is used to model the compressible unsteady flow governed by the Reynolds-averaged Navier Stokes (RANS) equations. ANSYS CFX utilizes a finite volume approach that yields a near second-order accurate spatial discretization. A second-order accurate backward Euler time-integration scheme is used for the unsteady calculations. The k-ϵ turbulence model is employed and scalable wall functions are used to resolve the near-wall boundary layer. The fluid is assumed to be ideal and calorically perfect. Further details of the ANSYS CFX solver are available in the ANSYS CFX-Solver Theory Guide.[27]

The CFD calculation is restricted to an isolated fan stage suitable for prediction of the unsteady aerodynamic characteristics of a bird-damaged fan. The fan stage starts downstream of the engine inlet, extends into the bypass duct and core duct, and includes a set of fan blades, a rotating hub, a stationary shroud, and a stationary splitter, as illustrated by Fig. 3. At the domain inflow, the total pressure, total temperature,

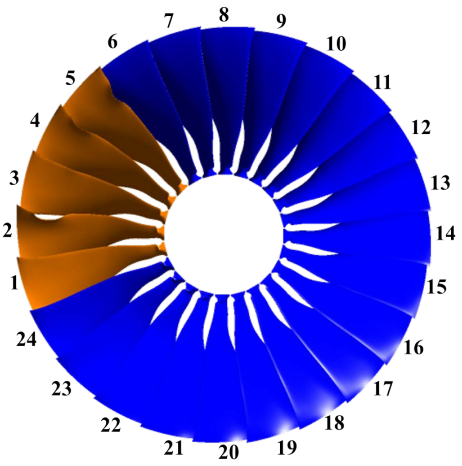

Figure 2. Bird-damaged fan configuration.

turbulence intensity, and direction of the incoming flow are enforced. The mass flow rate is specified at the core duct outflow with the assumption that the engine core "pulls" a fixed mass flow rate through the core duct for a given engine rotation speed. Static pressure is enforced at the bypass duct outflow using a radial-equilibrium condition that permits the static pressure to vary radially while maintaining the specified static pressure on average. Solid wall boundary conditions are enforced at the fan blades, hub, shroud, and splitter such that the velocity of the flow matches that of the wall through specification of a no-slip condition. A zero wall velocity is prescribed at the shroud and splitter, and a non-zero wall velocity that results from engine rotation is prescribed at the blades and hub.

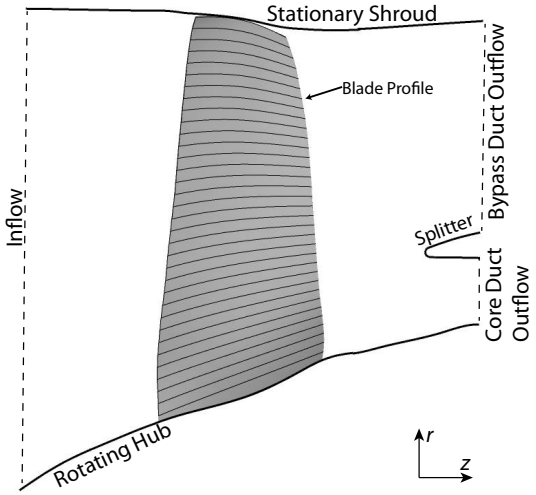

Figure 3. Meridional cross-section of the fan stage computational domain.

A. Operating Condition

The operating point of a fan stage is characterized by the total pressure ratio and referred mass flow rate. The total pressure ratio is defined as the ratio of the mass flow averaged total pressure at the bypass duct outflow to the mass flow averaged total pressure just upstream of the fan blades. The referred mass flow rate, calculated using Eq. (1), is the mass flow rate through the domain corrected for non-standard day inflow conditions and represents the mass flow that would pass through the fan if the inflow total pressure and total temperature corresponded to standard day conditions.

$$\dot{m}_R = \dot{m}\sqrt{\frac{T}{T_{STD}}}\left(\frac{P_{STD}}{P}\right) \tag{1}$$

A fan map depicts the operating points of an isolated fan stage for a variety of operating conditions. The operating points obtained at a fixed engine speed are connected to form characteristic curves. The stall point is identified by the peak in total pressure ratio along a characteristic curve and indicates the onset of stall. Stall is an undesirable, unsteady flow phenomena produced by flow separation that typically occurs at low mass flow rates and high bypass duct static pressure. A stall line connects the stall points on each characteristic curve and identifies the boundary of steady flow, where operating points to the left of the stall line are unsteady. A fan map also includes the fan operating line that consists of the unique set of operating points produced by the fan stage when installed in a complete engine. A representative fan map that includes an operating line, several characteristic curves, and the associated stall points is shown in Fig. 4.

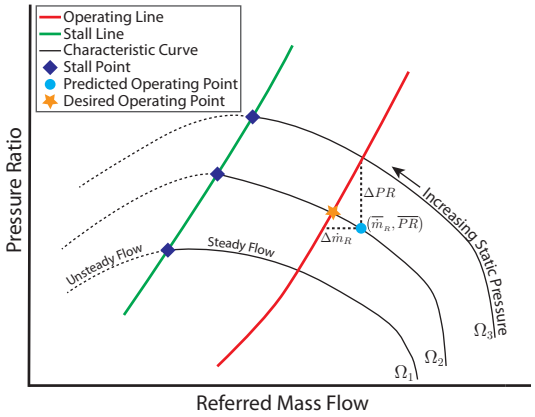

Figure 4. Representative fan map.

The operating points at the intersection of the operating line and the characteristic curves are significant because they represent operation of the isolated fan stage in a complete engine. The bypass duct static pressure boundary condition is specified so that the predicted operating point coincides with a point on the operating line. The bypass duct static pressure necessary to achieve the desired operating point at the intersection of the characteristic curve and the operating line is unknown a priori. Therefore, an iterative procedure is utilized to map the characteristic curve and determine the bypass duct static pressure that yields an operating point within ~3% error of the operating line. The error is calculated using Eq. (2) where the predicted operating point is denoted by $\left(\overline{\dot{m}}_R, \overline{PR}\right)$, and $\Delta\dot{m}_R$ and ΔPR denote the horizontal and vertical distance of the operating point from the operating line, as shown in Fig. 4.

$$\%\Delta\mathrm{OL} = \sqrt{\left(\frac{\Delta\dot{m}_R}{\overline{\dot{m}}_R}\right)^2 + \left(\frac{\Delta PR}{\overline{PR}}\right)^2} \times 100 \tag{2}$$

B. Computational Mesh

The ANSYS TurboGrid program is employed to generate a high-quality, structured CFD mesh of hexahedral elements for an undamaged blade passage. Mesh sensitivity studies were conducted in Ref. 28, and it was concluded that the "coarse" mesh identified in Ref. 28 is sufficiently accurate for the objectives of the current study. The ANSYS TurboGrid ATM topology is not applicable for full wheel geometries that include a set of damaged blades. To extend the high mesh quality produced by the ANSYS Turbo Grid ATM mesh topology to the damaged fan geometry, the automated mesh deformation scheme presented in Ref. 28 is utilized. A constant-span cross-section at 75% blade span is shown in Fig. 5(a), and an overall meridional view of the computational mesh of the mesh for a single blade passage is depict in Fig. 5(b). The full wheel mesh consists of 10.4 million nodes and 9.7 million elements.

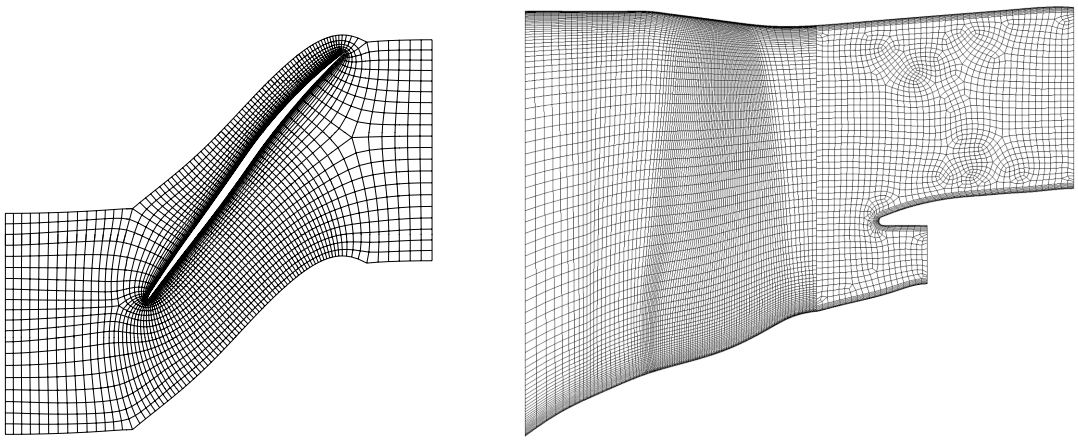

(a) CFD mesh at 75% blade span.

(b) Meridional view of CFD mesh.

Figure 5. Constant-span and meridional cross-sections of the CFD mesh.

IV. Structural Dynamic Model

The structural dynamic model is implemented in ANSYS Mechanical APDL, a commercially available FE-based structural solver that accommodates one-way and two-way coupling with ANSYS CFX for the forced response and aeroelastic response calculations performed in this study. Details of ANSYS Mechanical APDL are available in the ANSYS Mechanical APDL Theory Reference Guide.[29] The computational domain for the structural dynamic model consists of 24 individual blades each cantilevered at the blade root. Fan blades of modern high bypass ratio commercial turbofans are significantly more flexible than the hub disks; therefore, the hub disk is not modeled and structural coupling between the fan blades is ignored.[17] Furthermore, residual stress and strain hardening of the damaged blades resulting from the bird impact is also neglected. The fan blades are assumed to be made of titanium and are modeled with a linearly elastic, isotropic material law.

A. Equations of Motion

The equations of motion are formulated from the principle of virtual work and solved by ANSYS Mechanical APDL. The equations of motion are given by Eq. (3), where $\mathbf{F}_{\Omega}$ represents the centrifugal effects due to engine rotation, and $\mathbf{F}_{\text{aero}}$ represents the aerodynamic force transferred from the CFD mesh. The global mass and stiffness matrices are assembled for the entire structural mesh using conventional finite element methods. For simplicity of the structural dynamic model, no structural damping is implemented. The assembled deformation vector, $\mathbf{U}$, contains the translational degrees of freedom for each node.

$$\mathbf{M}\ddot{\mathbf{U}} + \mathbf{K}\mathbf{U} = \mathbf{F}_{\Omega} + \mathbf{F}_{\text{aero}} \tag{3}$$

The implementation of the structural dynamic model in ANSYS Mechanical APDL includes a large deflection formulation that is limited to geometric nonlinearity. This is accomplished by a geometric stiffness matrix where the radial loading depends on the speed of rotation and distance of the element from the axis of rotation. A Newton-Raphson iterative procedure is implemented to update the stiffness matrix within each time-step. The HHT-α[30] time-integration scheme is used to integrate Eq. (3) in time. Further details on the Newton-Raphson algorithm and the HHT-α scheme are provided in the ANSYS Mechanical APDL Theory Reference Guide.[29]

B. Computational Mesh

The fan blades are modeled using 8-noded, solid, hexahedral elements (ANSYS SOLID185 element type) with three translational degrees of freedom at each node. A mesh sensitivity was conducted in Ref. 28 to identify the mesh resolution suitable for the objectives of this study. The structural mesh consists of 5,712

nodes and 4,020 elements per blade for a total of 137,088 nodes and 96,480 elements for the full wheel model. Figure 6 shows the structural mesh of an undamaged blade.

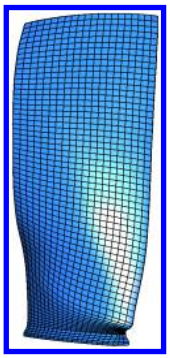

Figure 6. Structural mesh for an undamaged blade.

C. Rotating Mode Shapes

The first 5 mode shapes of a rotating, undamaged fan blade at 100% take-off engine rotational speed are shown in Figs. 7. The mode shapes of a rotating, undamaged blade at 75% and 60% take-off thrust are similar in shape. The mode shapes of the damaged blades are similar to those of the undamaged blade. Note that the frequencies and mode shapes described in Fig. 7 have been identified as "1st bending (1B)", "2nd bending (2B)", etc.. However, due to the built-in twist of the blade and the effect of rotation, these modes are coupled where all three degrees of freedom (bending out of the plane of rotation, bending in the plane of rotation, and torsion) participate. By identifying the mode as "1B" it is implied that the primary contribution to the mode shape comes from bending.

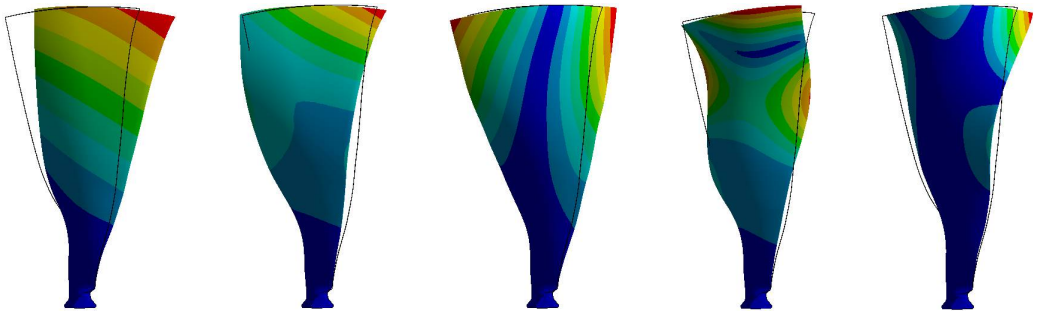

(a) 1st bending (1B). (b) 2nd bending (2B). (c) 1st torsion (1T). (d) 3rd bending (3B). (e) 2nd torsion (2T).

Figure 7. First 5 mode shapes of a rotating, undamaged blade.

V. Coupled Fluid-Structure Framework

The ANSYS Multi-field solver is used to couple the ANSYS CFX aerodynamic solver and ANSYS Mechanical APDL structural solver for the forced response and aeroelastic response calculations performed in this study. The computational frameworks and coupling algorithm for the one-way and fully-coupled fluid-structure interaction calculations are provided next. Further details of the coupled fluid-structure framework, including the aerodynamic load transfer and mesh deformation scheme, is available in Ref. 28. Information regarding the coupling algorithm and mesh mapping scheme is available in the ANSYS MFX documentation.[31]

A. One-way Forced Response Framework

For the one-way forced response calculation, the unsteady aerodynamic loads are calculated and applied to the structural model at each time-step to obtain the response. For this case, the CFD mesh is not deformed as the structure deforms; therefore, the feedback mechanism of the structural response on the unsteady aerodynamic loading is not captured. The aerodynamic load for the forced response is time dependent and thus it captures the transient nature of the aerodynamic loading. Equation (4) governs the forced response calculations.

$$\mathbf{M}\ddot{\mathbf{U}} + \mathbf{K}\mathbf{U} = \mathbf{F}_{\Omega} + \mathbf{F}_{\text{aero}}(t) \tag{4}$$

A flow chart of the forced response framework is shown in Fig. 8. The mapping between the FE mesh and the CFD mesh at the wetted surface is performed to establish the fluid structure interface (FSI). A steady-state CFD calculation is carried out to generate the initial conditions for the unsteady CFD calculations needed for the forced response calculation. During each time-step of the forced response calculation, the aerodynamic pressure and viscous loads from the unsteady CFD analysis are transferred to the surface of the FE mesh and the structural dynamic response is calculated.

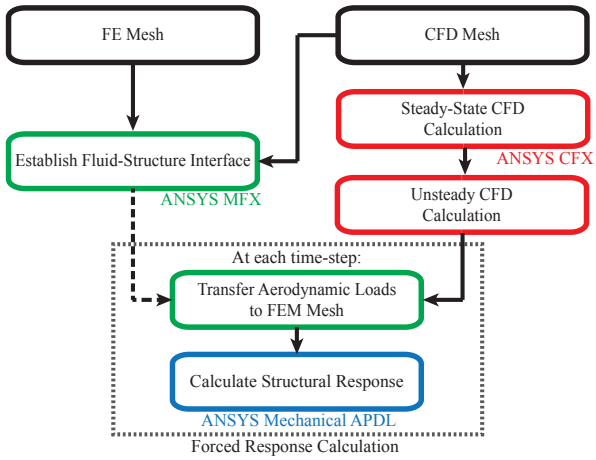

Figure 8. Flow chart of the forced response framework.

B. Fully-Coupled Aeroelastic Framework

To obtain the coupled fluid-structure aeroelastic response, an implicit coupling algorithm is employed where the aerodynamic and structural components representing the fan are solved iteratively in each time-step. The CFD mesh is deformed with the structure such that the time-varying displacement at the blade surface influences the aerodynamic loads on the structure. The aerodynamic load varies with time due to the transient effects in the aerodynamic loading caused by both the bird damage and the blade motion. The equations governing the aeroelastic response calculations are provided by Eq. (5).

$$\mathbf{M}\ddot{\mathbf{U}} + \mathbf{K}\mathbf{U} = \mathbf{F}_{\Omega} + \mathbf{F}_{\text{aero}}(t, \mathbf{U}, \dot{\mathbf{U}}, \ddot{\mathbf{U}}) \tag{5}$$

A flow chart of the fully-coupled aeroelastic framework is shown in Fig. 9. The mapping between the FE mesh and the CFD mesh is performed to establish the FSI at the wetted surface. Next, the aerodynamic forces from a steady-state CFD calculation of the damaged fan are applied to a static structural model to initialize the aerodynamic load and structural dynamic model for the aeroelastic response calculations. Within each time-step of the aeroelastic response calculation, the aerodynamic state is calculated and the associated aerodynamic loads are transferred to the FE mesh. The resulting structural displacements are then transferred to the CFD mesh blade surface and the interior CFD nodes are displaced by the amount dictated by the structural deformation.

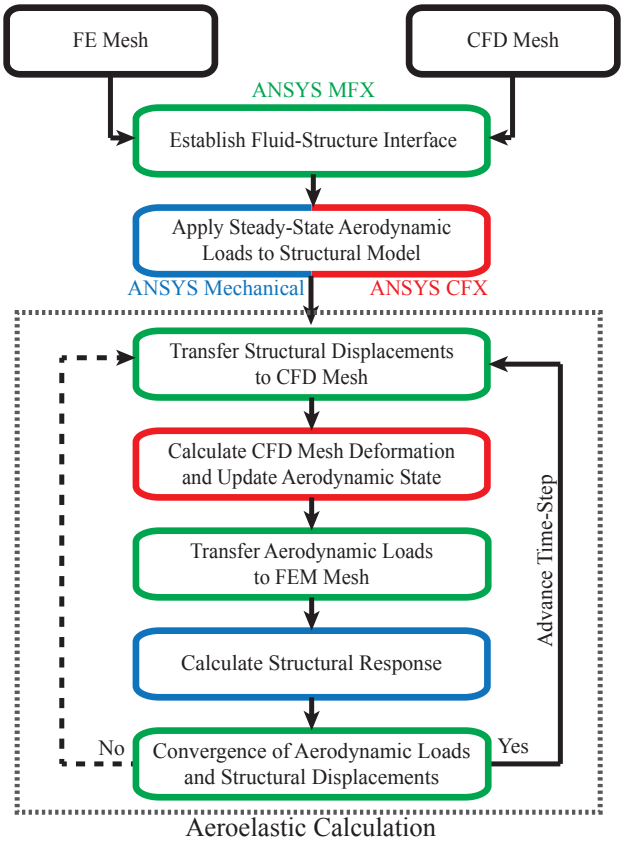

Figure 9. Flow chart of the aeroelastic framework.

VI. Results

The steady and unsteady aerodynamic calculations of the bird-damaged fan operating at the 100%, 75%, and 60% throttle settings are presented in this section. Subsequently, the forced response and aeroelastic response of a bird-damaged fan at these three operating conditions are presented and compared to determine the role of aeroelastic coupling. The aerodynamic work calculated from the forced response and aeroelastic response calculations are compared to identify the potential for aeroelastic instability. Reference 28 provides further details of the methodology and results.

1. Aerodynamic Calculations of the Damaged Fan

Steady-state and unsteady aerodynamic calculations are used to provide insight into the aerodynamic characteristics of the bird-damaged fan. The freestream conditions correspond to standard day +27°F conditions and the freestream flight Mach number is zero. In Ref. 28, steady-state aerodynamic calculations performed with the aerodynamic model were verified against data from industry for an undamaged and damaged fan.

2. Steady-State Aerodynamic Calculations

Steady aerodynamic calculations were performed at the 100%, 75%, and 60% throttle settings to gain insight into the aerodynamic behavior of the damaged fan and also to provide the initial conditions for the unsteady aerodynamic calculations. The characteristic curves of the damaged fan were mapped for each throttle setting by varying the bypass duct static pressure. The bypass duct static pressure was gradually increased to reach an operating point near the operating line that represents operation of the damaged fan installed in a complete engine. Figure 10 provides the fan map of the damaged fan and includes the fan operating line and the characteristic curves corresponding to the 100%, 75%, and 60% throttle settings. The values in Figs. 10 are normalized by the undamaged fan operating point at the 100% throttle setting. It is important to

note that the steady calculations converge at a "snap-shot" of the unsteady behavior that may not represent completely the time-averaged behavior of the unsteady solution.

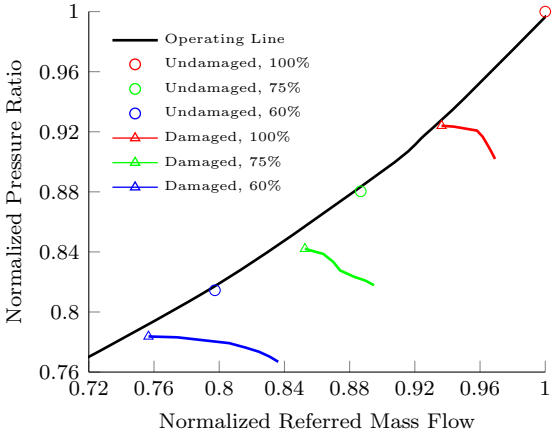

Figure 10. Damaged fan map for 100%, 75%, and 60% throttle settings.

The damaged fan map clearly illustrates the significant influence of the bird damage on the steady aerodynamic behavior of the damaged fan. The damaged fan characteristic curves are much flatter near the operating line, indicating that the damaged fan is operating very near the stall point where unsteady flow phenomena may be significant. The operating point of the damaged fan is also significantly affected by the bird damage. Table 2 compares the undamaged and damaged operating points, normalized by the operating point of the undamaged fan at the 100% throttle setting. Table 2 also provides the percent mass flow loss relative to the undamaged fan at the corresponding throttle setting, where the mass flow loss is related to the thrust loss resulting from the bird strike. To calculate the mass flow loss for the 75% and 60% throttle settings, the characteristic curve is extrapolated to the operating line assuming a constant pressure ratio (i.e. flat characteristic curve). The largest mass flow loss occurs for the 100% and 60% throttle settings followed by the 75% throttle setting.

Table 2. Comparison of operating points for the undamaged and damaged fan.

Throttle Setting	Configuration	Normalized $\dot{m}_R$	Normalized PR	% Flow Loss	%ΔOL
100%	Undamaged	1.000	1.000	N\A	0.22%
100%	Damaged	0.931	0.933	7.33%	0.63%
75%	Undamaged	0.881	0.889	N\A	0.70%
75%	Damaged	0.847	0.850	5.90%	3.3%
60%	Undamaged	0.793	0.822	N\A	0.74%
60%	Damaged	0.752	0.791	7.20%	2.5%

3. Unsteady Aerodynamic Calculations

The unsteady aerodynamic calculations for the 100%, 75%, and 60% throttle settings are initialized from the corresponding steady solution. A physical time-step corresponding to 500 time-steps per revolution is specified, and 3 CFD-solver sub-iterations are performed at each time-step for convergence of the solution. The unsteady calculations were performed for 5,000 time-steps corresponding to 10 revolutions of the fan.

The unsteady operating point is plotted on the fan map in Figs. 11(a), 11(b), and 11(c), where the values are normalized by the referred mass flow rate and total pressure ratio of the undamaged fan at the same throttle setting. Considerable unsteadiness in the operating point is evident. For the 100% and 60% throttle settings, the unsteady operating point oscillates about the steady operating point, and the unsteady

operating point for the 75% throttle setting oscillates about a point below the steady value. The mean flow loss is approximately 8% for each case, and is greater than that predicted by the steady calculations for the 75% and 60% throttle settings. Furthermore, the 75% throttle setting exhibits the largest flow loss of 8.4% and is considerably greater than the 5.9% flow loss predicted by the steady solution. Therefore, it is clear that unsteady effects are important in predicting the flow loss of the damaged fan, and the steady aerodynamic calculation of the damaged fan tends to under-predict the flow loss.

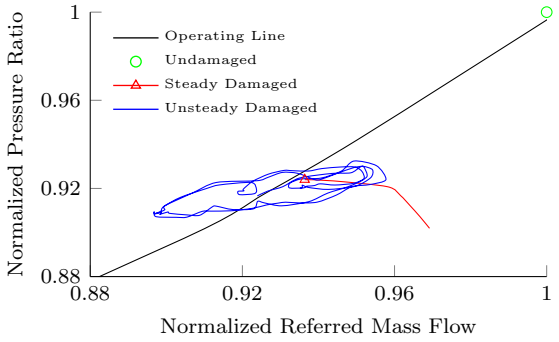

(a) Fan map with characteristic curve and steady and unsteady operating points at the 100% throttle setting.

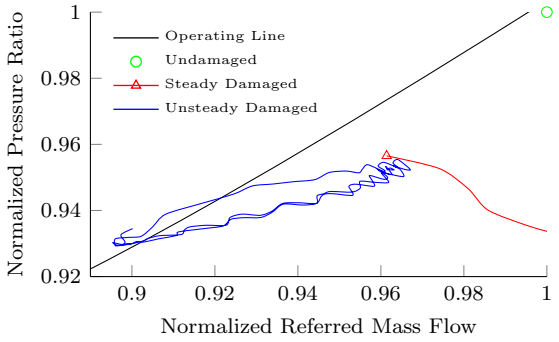

(b) Fan map with characteristic curve and steady and unsteady operating points at the 75% throttle setting.

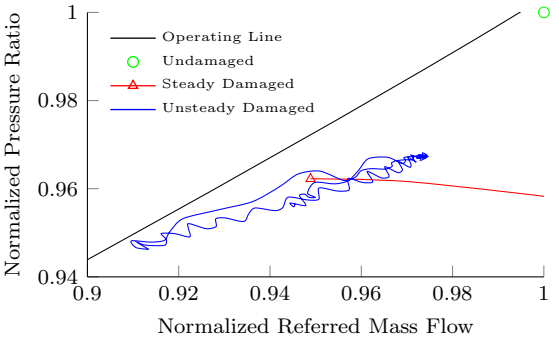

(c) Fan map with characteristic curve and steady and unsteady operating points at the 60% throttle setting.

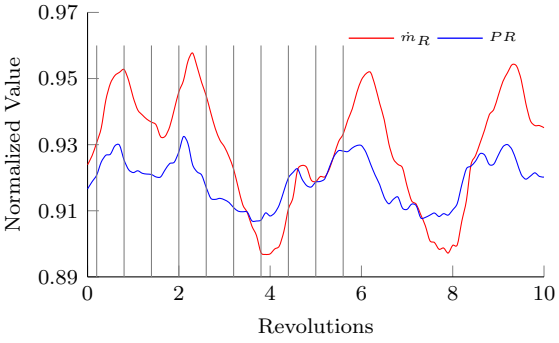

(d) Referred mass flow rate and total pressure ratio time history at the 100% throttle setting.

Figure 11. Unsteady total pressure ratio and referred mass flow rate.

Mach contours at mid-chord are examined to provide insight into the unsteady behavior of the damaged fan. Figures 12 depicts the unsteady Mach number contours at the mid-chord for 10 equally spaced time-steps spanning one representative oscillation of the unsteady solution at the 100% throttle setting. The corresponding total pressure ratio and referred mass flow rate at these time-steps are indicated by the fine vertical lines in Fig. 11(d). Only a small amount of unsteadiness is observed in the vicinity of the damaged blades where the flow remains largely separated, and the flow through the damaged blade passages is partially or totally blocked. By contrast, considerable unsteadiness is evident in much of the undamaged sector, with the greatest level of flow unsteadiness occurring in the blade passages between blade 16 clockwise to blade 21.

The stalled flow emanating from the damaged sector, denoted a stall cell and identified by the blue regions, is the dominant unsteady flow effect in Figs. 12. At 0.8 revolutions, the stall cell covers roughly a third of the fan wheel, from blade 21 clockwise to blade 5, and the mass flow rate is near its maximum. From 1.4 revolutions to 3.8 revolutions, the stall cell regresses slightly before propagating opposite to the direction of rotation until half of the blade tips are stalled, from blade 15 clockwise to blade 5. At this point, the mass flow rate is at a minimum due to the partially blocked blade passages associated with the stalled flow. Subsequently from revolution 4.4 to revolution 5.6, the stall cell detaches from the damaged sector, progresses opposite the direction of rotation, and dissipates as the flow recovers and the mass flow rate increases to the maximum value. Furthermore, as the stall cell propagates at the blade tips, the Mach number in the inner span of the corresponding blade passage also decreases, indicating a loss of mass flow through most of the blade passages.

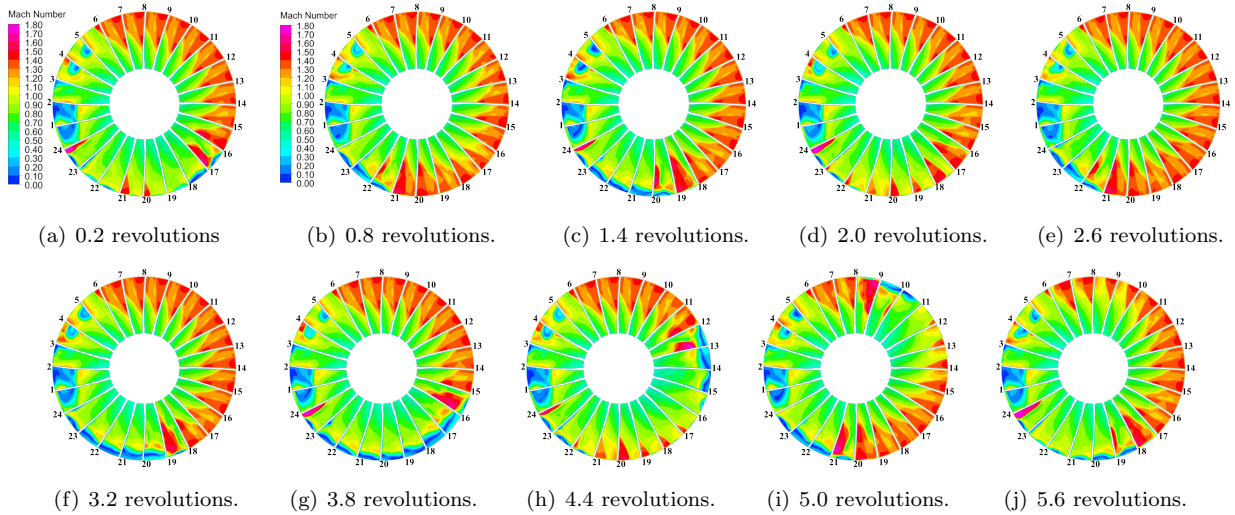

(a) 0.2 revolutions (b) 0.8 revolutions. (c) 1.4 revolutions. (d) 2.0 revolutions. (e) 2.6 revolutions.

(f) 3.2 revolutions. (g) 3.8 revolutions. (h) 4.4 revolutions. (i) 5.0 revolutions. (j) 5.6 revolutions.

Figure 12. Unsteady mid-chord Mach number contours of the damaged fan at the 100% throttle setting (direction of rotation: clockwise).

The unsteady Mach contours at 60% and 75% throttle setting are similar to the 100% case and are provided in Ref. 28. Similar to the 100% case, the dominant unsteady property is the stalled flow emanating from the damaged sector. For the 75% and 60% throttle setting, the stall cell at the blade tips propagates opposite to the direction of rotation until the mass flow rate is at a minimum. As the mass flow rate recovers, the stall cell regresses in the direction of rotation. The stall cell does not detach from the damaged sector, as is the case for the 100% throttle setting, and the stall cell extends counterclockwise to blade 12. The Mach number of the unstalled blade passages between blades 6 and 11 also varies considerably with the progression and regression of the stall cell.

A. Forced Response of the Damaged Fan

The forced response calculations of the bird damaged fan at the 100%, 75%, and 60% throttle settings are presented in this section. The time-dependent aerodynamic loads are extracted from the unsteady CFD calculations and transferred to the structural solver at each time-step using the one-way forced response framework. The calculations were performed for 5,000 time-steps corresponding to 10 revolutions of the fan. The circumferential displacement, $u_\theta R$, at the blade tip leading edge is used to illustrate the structural response time-history. The displacement is calculated relative to the running configuration.

Figure 13(a) shows the tip displacement for the duration of the forced response calculation at the 100% throttle setting for four representative blades. Blade 5 represents the responses of the damaged blades 1-5, blade 12 the responses of blades 6-14, blade 18 the responses of blades 15-21, and blade 24 the responses of blades 22-24. Responses for the remaining blades are available in Ref. 28. The largest tip displacements occur for blades 15-21, as illustrated by blade 18, which grow in time and result from the large aerodynamic loads produced by the unsteady stall cell in this region of the fan. The tip displacements for blades 6-14, illustrated by blade 12, exhibit a limited structural response for the first 4 revolutions until the stall cell releases from the damaged sector and progresses through this region of the fan producing a sudden increase in tip displacement. The behavior is repeated at ∼8 fan revolutions when a second stall cell is released and progresses through this region. By comparison, blades 22-24, which are located immediately downstream of the damaged sector, exhibit smaller tip displacements that is limited with time, as illustrated by blade 24 in Fig. 13(a). Finally, the tip displacements of the damaged blades 1-5, illustrated by blade 5, are the smallest with blade 4 exhibiting the largest response among the 5 damaged blades. The most significant structural response occurs for the blades opposite the damaged sector due to the progression of the stall cell.

The circumferential displacements of the blade tips for the 75% and 60% throttle settings are shown in Figs. 13(b) and 13(c) for four representative blades. Blade 4 represents the responses of the damaged blades 1-5, blade 11 the responses of blades 6-11, blade 14 the responses of blades 12-19, and blade 24 the responses of blades 20-24. The tip displacements are similar for the two throttle settings. The tip displacements for

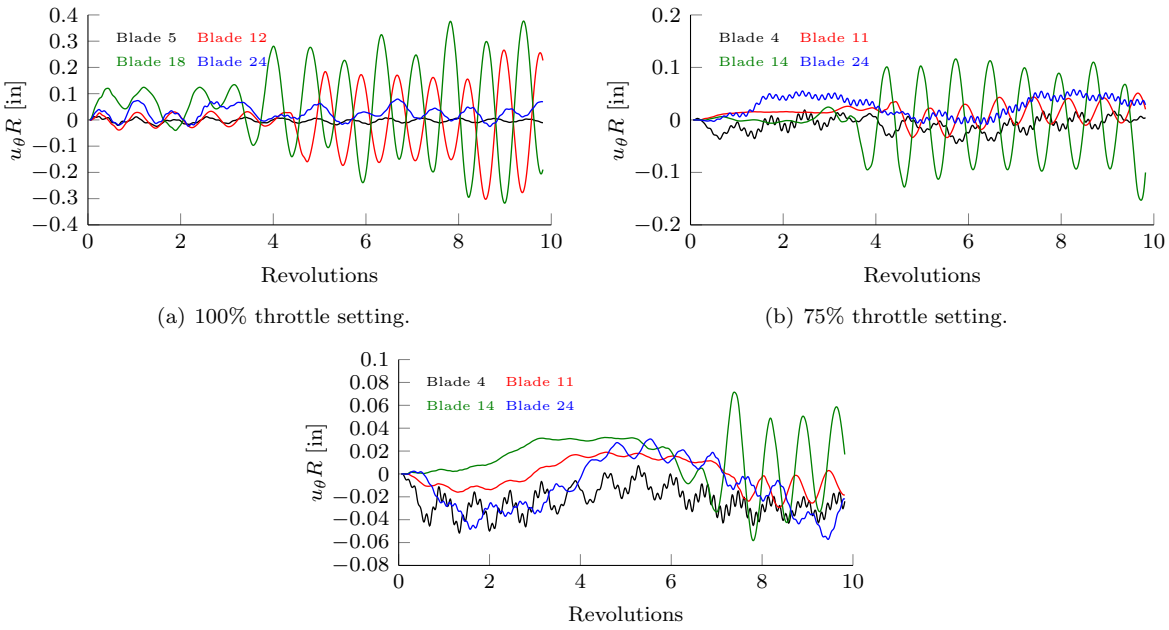

(a) 100% throttle setting.

(b) 75% throttle setting.

(c) 60% throttle setting.

Figure 13. Tip displacements from the forced response calculations, relative to the steady-state configuration.

blades 12-19, illustrated by blade 14 in Figs. 13(b) and 13(c), are the greatest and result from the progression and regression of the stall cell in this region of the fan. For both cases, the tip displacement of blade 14 initially exhibits a limited response until the stall cell released from the damaged sector progresses through this region of the fan at ∼4.5 revolutions. Comparing these cases with the 100% throttle setting, it is evident that the unsteady stall cell does not detach and propagate through the undamaged blades 6-11 upstream of the damaged sector. Therefore, the tip displacements of these blades, illustrated by blade 11, are the smallest and appear to be excited primarily by the cyclic increase and decrease of mass flow through these blade passages. The tip displacements of blades 20-24, which are located immediately downstream of the damaged sector, are illustrated by blade 24 in Figs. 13(b) and 13(c). Blade 24 displays a structural response at higher frequency and smaller amplitude that is induced by the unsteady wake shed from the damaged sector. Finally, the tip displacements of the damaged blades 1-5, illustrated by blade 5, also exhibit a higher frequency content. For both cases, blades 3 and 4 display the largest structural response among the damaged blades.

To determine the modal participation in the structural response, the blade displacements are projected into modal coordinates using Eq. (6). During post-processing of the structural response, Eq. (6) is solved at each time-step using a least squares approach to determine the generalized degrees of freedom, q_m, corresponding to each mode shape. In this process, the first 10 natural modes of each rotating blade are used and the mode shapes are normalized by the magnitude of the leading edge tip displacement. Subsequently, Eq. (7) is used to calculate the contribution of the m^{th} natural mode to the displacement of any node in the FE mesh.

$$\mathbf{U}(\mathbf{x},t) \approx \sum_{m=1}^{10} q_m(t)\Phi_m(\mathbf{x}) \tag{6}$$

$$\mathbf{U}_m(\mathbf{x},t) = q_m(t)\Phi_m(\mathbf{x}) \tag{7}$$

Table 3 summarizes the modal contribution of the forced response of blades 1-24 at each throttle setting. In Table 3, bold face type indicates the dominant modes, ↓ indicates a decaying mode, ↑ indicates a growing mode, and * indicates a mode whose amplitude displays beating. Overall, the first bending mode dominates the response of the blades at each throttle setting. In addition, the tip displacements of the damaged blades 1-5 contain contributions from the first torsion mode, which decays in time, together with the third

bending and second torsion modes that exhibit beating. For the 100% throttle setting, the response of the undamaged blades is exclusively in the first bending mode, with the exception of blade 24 that includes a small contribution from the second torsion mode. The first bending mode also dominates the response of the undamaged blades for the 75% and 60% throttle cases. However, the first torsion and second bending modes also contribute to the response of the upstream undamaged blades, and the second torsion mode displays beating in the region downstream of the damaged blades.

Table 3. Summary of modal contributions of the first 5 rotating modes for the forced response calculations.

	100% Throttle Setting	75% Throttle Setting	60% Throttle Setting
Blade 1	**1B**	**1B**, 2T*	**1B**, 2T*
Blade 2	**1B**, 1T↓	**1B**, 2T*,3B*	**1B**, 1T↓, 3B*, 2T*
Blade 3	**1B**, 1T↓, 2T*	**1B**, **2T***	**1B**, 2T*
Blade 4	**1B**, 1T↓, 2T*	**1B**, **2T***, 1T↓, 3B*	**1B**, **2T***, 1T↓, 3B*
Blade 5	**1B**, 1T↓, 2T*	**1B**, **2T***, 1T↓, 3B*	**1B**, **2T***, 3B*
Blade 6-11	**1B**↑	**1B**↑, 2B, 1T	**1B**↑, 2B, 1T
Blade 12-19	**1B**↑	**1B**↑, 2T*	**1B**↑, 2T*
Blade 20	**1B**↑	**1B**, 2T*	**1B**, 2T*
Blade 21	**1B**↑	**1B**, 2T*	**1B**, 2T*
Blade 22-23	**1B**	**1B**, 2T*	**1B**, 2T*
Blade 24	**1B**, 2T*	**1B**, **2T***	**1B**, 2T*

B. Aeroelastic Response of the Damaged Fan

The aeroelastic response calculations of the bird damaged fan at 100%, 75%, and 60% throttle setting are presented in this section. The aerodynamic and structural models are solved iteratively within each time-step using the fully-coupled aeroelastic framework. The calculations are performed with 500 time-steps per revolution for 10 fan revolutions.

The circumferential displacement at the leading edge of the blade tips is presented in Fig. 14(a) for the aeroelastic response calculation at the 100% throttle setting. The displacement is calculated relative to the steady-state configuration, and the responses of blades 5, 12, 18, and 24 represent blades 1-5, 6-11, 12-19, and 20-24, respectively. Responses for the remaining blades are available in Ref. 28. The aeroelastic response of the undamaged fan blades resembles the forced response. The largest tip displacements occur for blades 15-21 and grow in time, as illustrated by blade 18. However, the amplitude of tip displacement for these blades is smaller than that from the forced response calculations. The responses of blades 6-14, illustrated by blade 12, exhibit a limited response for the first ∼3.5 revolutions until the stall cell releases from the damaged sector and progresses through this region of the fan producing a sudden increase in tip displacement. After the increase in blade response at ∼3.5 revolutions, the tip displacements decay more rapidly than for the forced response case, indicating that the aeroelastic coupling introduces positive damping for these blades. The response of blades 22-24 displays smaller tip displacements that remain bounded with time, as illustrated by blade 24. When compared to the forced response results in Fig. 13(a), the tip displacements for blades 22-24 contain a higher frequency content indicating that higher structural modes are participating in the response of these blades. The tip displacements of the damaged blades 1-5, as illustrated by blade 5 in Fig. 14(a), are the smallest; however, the aeroelastic response of these blades also contains a higher frequency component compared to the forced response calculation shown in Fig. 13(a).

The circumferential displacement of the blade tips for the 75% throttle setting is presented in Fig. 14(b). The largest tip displacements occur for blades 12-19 and are due to the stall cell at the blade tips, as illustrated by blade 14. The tip displacements for blades 6-11, illustrated by blade 11, are larger than those from the forced response calculations and result from the unsteady stall cell that extends further around the wheel than in the forced response case. The response of blades 20-24 exhibit a slightly larger structural response compared to the forced response calculations, as illustrated by blade 24. The tip displacements of

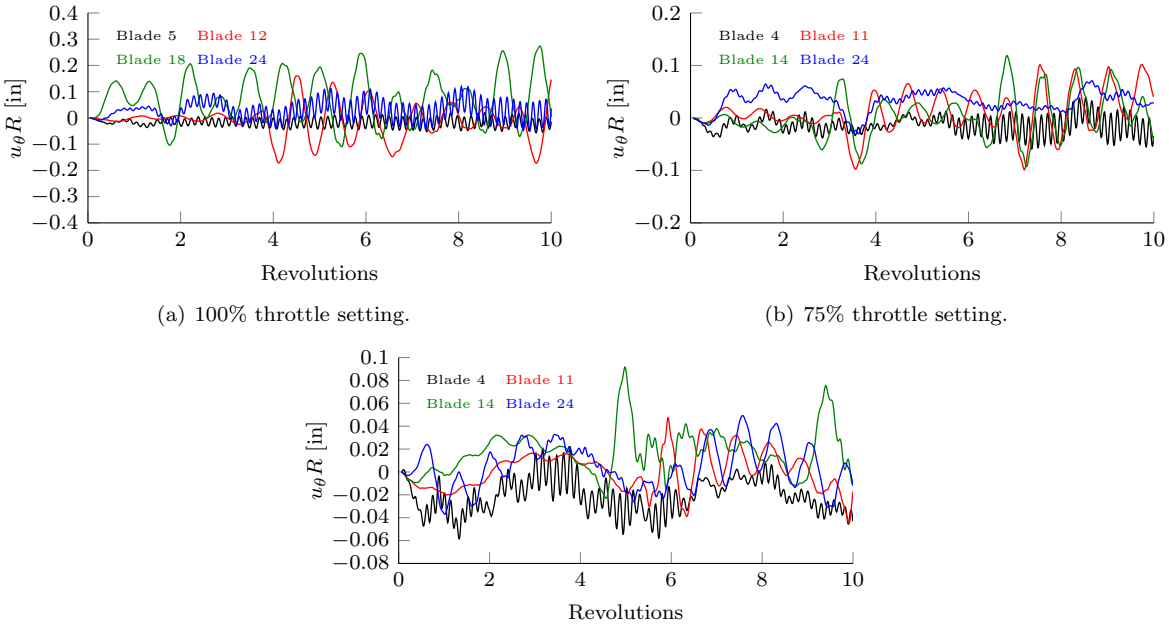

(a) 100% throttle setting.

(b) 75% throttle setting.

(c) 60% throttle setting.

Figure 14. Tip displacements from the aeroelastic response calculations, relative to the running configuration.

the damaged blades 1-5, illustrated by blade 4, display a higher frequency content indicating the participation of a higher structural modes.

The circumferential displacement of the blade tips for the 60% throttle setting is presented in Fig. 14(c). The largest tip displacements occur for blades 12-19, as illustrated by blade 14. The structural response of these blades exhibit a higher frequency content than the forced response calculations, particularly after the stall cell progresses at ∼3.5 revolutions. Blades 6-11, illustrated by blade 11, display limited response until the stall cell detaches and progresses through this region of the fan at ∼5.0 revolutions. When compared to the forced response calculations, the increase in tip displacements is larger and occurs earlier. The structural response of blades 20-24, illustrated by blade 24, are similar to the forced response case with the exception of higher frequency content that appears after ∼4 revolutions. Similar to the aeroelastic response calculations at 100% and 75% throttle settings, the tip displacements of the damaged blades 1-5, represented by blade 4, also display a higher frequency content compared to the forced response.

Table 3 summarizes the modal contribution for the aeroelastic response of blades 1-24 at each throttle setting. The first bending mode is dominant in the forced and aeroelastic response of all blades, with the amplitude of this mode growing for the undamaged blades 6-18. The tip displacements from the aeroelastic response also contain increased contributions from higher modes that may be significant and may grow in time or exhibit beating. Comparison of the Tables 3 and 4 reveals some fundamental differences between the forced and aeroelastic response of the damaged fan. For forced response, the primary response of the blade is in the fundamental bending mode, with occasional participation of the higher modes primarily in the second torsion mode. The participation of the higher structural modes is much more evident in the aeroelastic response column, which is reasonable when recognizing that aeroelastic behavior often exhibits a coupled bending-torsion response.

The influence of aeroelastic coupling is illustrated by Figs. 15- 17 in which the modal contributions to the forced response and aeroelastic response are compared for one blade at each throttle setting. For the aeroelastic response of blade 24 at the 100% throttle setting, the second torsion mode grows rapidly in time and dominates the blade response after ∼2 fan revolutions, as shown in Fig. 15(b). The rapid growth of the second torsion mode is unique to the aeroelastic response and may indicate an aeroelastic instability. For the 75% throttle case, the influence of aeroelastic coupling is most evident in the aeroelastic response of blade 4, which exhibits a rapid growth of the second torsion mode as shown in Fig. 16(b). For the 60% throttle case, the effect of aeroelastic coupling on the circumferential tip displacement is evident, by the appearance

Table 4. Summary of modal contributions of the first 5 rotating modes for the aeroelastic response calculations.

	100% Throttle Setting	75% Throttle Setting	60% Throttle Setting
Blade 1	**1B**, **2T**↑	**1B**, 1T↓, 3B↓, 2T*	**1B**, 3B*
Blade 2	**1B**, 3B*, 2T*	**1B**, **3B***, **2T***	**1B**, **3B***, 2B, 1T↓, 2T*
Blade 3	**1B**, **2T**↑	**1B**, **2T***, 1T↓, 3B*	**1B**, 3B*, 2T*
Blade 4	**1B**, **2T***	**1B**, **2T**↑, 1T↓, 3B*	**1B**, **3B***, **2T***, 2B, 1T↓
Blade 5	**1B**, **2T**↑	**1B**, **2T**↑, 3B*	**1B**, **3B***, 1T↓, 2T*
Blade 6-8	**1B**↑	**1B**↑, 2B, 1T	**1B**↑, 2B, 1T
Blade 9	**1B**↑	**1B**↑, 2B, 1T	**1B**↑, 2B, 1T, 2T
Blade 10-11	**1B**↑	**1B**↑, 2B, 1T, 2T	**1B**↑, 2B, 1T, 3B, 2T
Blade 12	**1B**↑	**1B**↑	**1B**↑, **3B***, 2B, 1T, 2T
Blade 13	**1B**↑	**1B**↑, 3B*	**1B**↑, **3B***, 2B, 1T
Blade 14-18	**1B**↑	**1B**↑	**1B**↑, **3B***, 2B, 1T
Blade 19-20	**1B**↑, 2T↑	**1B**↑, 2T*	**1B**↑, **3B***, 2B, 1T
Blade 21	**1B**↑, 2T↑	**1B**↑, 2T*	**1B**, **3B***, 2B, 1T
Blade 22	**1B**, **2T**↑	**1B**↑, 2T*	**1B**, **3B***, 2B, 1T, 2T
Blade 23	**1B**, **2T**↑	**1B**↑, 2T*	**1B**, 1T, 2B, 3B↑, 2T
Blade 24	**1B**, **2T**↑	**1B**↑, 2T*	**1B**, 1T, 2B, 3B↑, 2T

and increased participation of the third bending mode. This is most noticeable in the aeroelastic response of blade 5, shown in Fig. 17(b), which is dominated by the first bending mode and displays an increased contribution from the third bending mode.

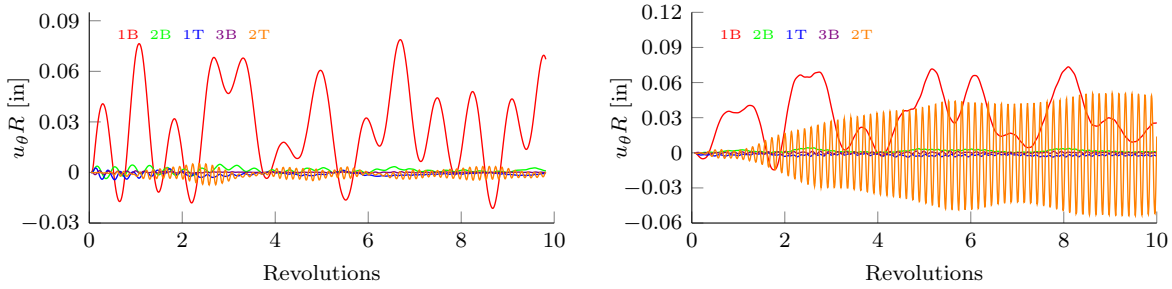

(a) Forced response.

(b) Aeroelastic response.

Figure 15. Comparison of blade tip modal contributions of blade 24 at 100% throttle setting.

C. Assessment of Aeroelastic Stability

The aeroelastic stability of the fan blades is difficult to determine due to the inherent unsteadiness of the aerodynamic environment caused by the bird damage. Common approaches to determine the aeroelastic stability of a structure often rely on calculating the aerodynamic damping associated with the growth or decay of the blade response. However, the unsteady aerodynamic loads associated with a bird damaged fan excite the blades causing a growth in blade response that may hide the aeroelastic effects.

To provide insight into the cause of the growing blade response in the aeroelastic response behavior, the work performed by the aerodynamic forces on the structure is calculated and compared to the forced response. The aeroelastic stability of the aeroelastic response is inferred based on the time-history of the aerodynamic work compared to the forced response calculations. Aerodynamic work that grows compared to the forced response indicates a potential aeroelastic instability. Aerodynamic work that decays compared

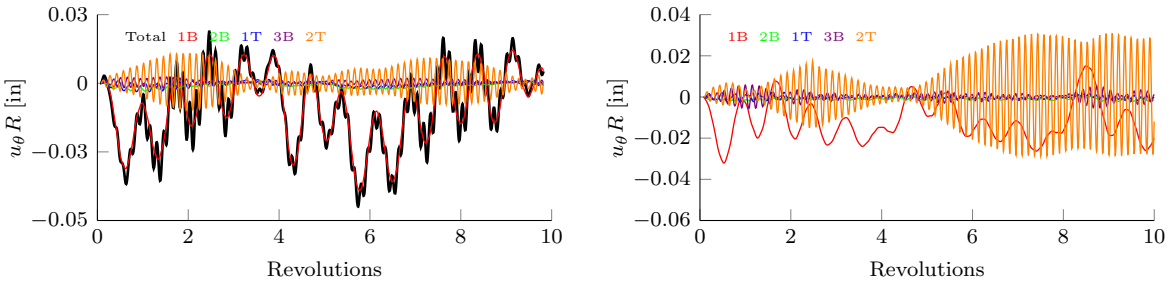

(a) Forced response. (b) Aeroelastic response.

Figure 16. Comparison of blade tip modal contributions of blade 4 at 75% throttle setting.

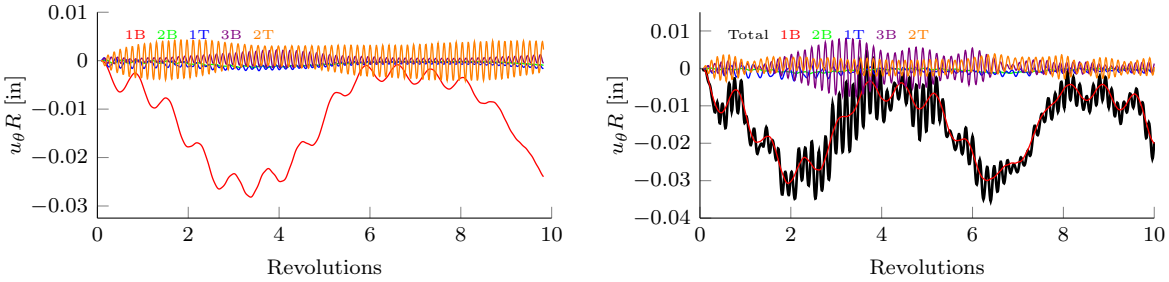

(a) Forced response. (b) Aeroelastic response.

Figure 17. Comparison of blade tip modal contributions of blade 5 at 60% throttle setting.

to the forced response calculations implies positive aerodynamic damping. The aerodynamic work of the entire blade is calculated for the forced and aeroelastic response using Eq. (8) and Eq. (9), respectively.

$$W_{FR}(t) = \int_0^t \mathbf{F}_{\text{aero}}(s) \cdot \dot{\mathbf{U}}(s) ds \tag{8}$$

$$W_{AR}(t) = \int_0^t \mathbf{F}_{\text{aero}}(s, \mathbf{U}, \dot{\mathbf{U}}, \ddot{\mathbf{U}}) \cdot \dot{\mathbf{U}}(s) ds \tag{9}$$

The aerodynamic work as a function of fan revolutions is presented in Figs. 18 for blades 5, 12, 18, and 24 at the 100% throttle setting. The aerodynamic work from the forced response is compared to aerodynamic work from the aeroelastic response to identify possible aeroelastic instabilities. In Fig. 18(a), the aerodynamic work on blade 5 from the aeroelastic response is positive and grows at a rate greater than that of the forced response indicating the potential for aeroelastic instability of the blade. The aerodynamic work for blade 24 from the aeroelastic response displays a behavior that resembles blade 5, as shown in Fig. 18(d), indicating a possible aeroelastic instability for this blade. For blades 12 and 18, the aerodynamic work from the aeroelastic response does not increase in time when compared to the forced response, as shown in Figs. 18(b) and 18(c). This suggests that the growth in response of these blades is due to the unsteady aerodynamic loads caused by the stall cell, and the aeroelastic effects introduce positive aerodynamic damping for these blades.

The aerodynamic work at 75% throttle setting is presented in Fig. 19 for blades 4, 11, 14, and 24. Comparison of the aerodynamic work on blade 4, shown in Fig. 19(a), indicates that the growth of the second torsion mode in the aeroelastic response of this blade may be indicative of an aeroelastic instability. For blades 11 and 14, the aerodynamic work from the aeroelastic response is similar to that from the forced response, as shown in Figs. 19(b) and 19(c). Therefore, the growth in response of these blades is due to the unsteady aerodynamic loads caused by bird damage rather than an aeroelastic instability. The aerodynamic work from the aeroelastic response for blade 24, shown in Fig. 19(d), is smaller when compared to the forced response. This suggests that aeroelastic effects introduce positive damping, which is evident by the decreased participation of the second torsion mode for the aeroelastic case.

Figures. 20 provides the aerodynamic work from the aeroelastic and forced response at the 60% throttle setting. The aerodynamic work for blade 5 is shown in Fig. 20(a). The aerodynamic work from the aeroelastic

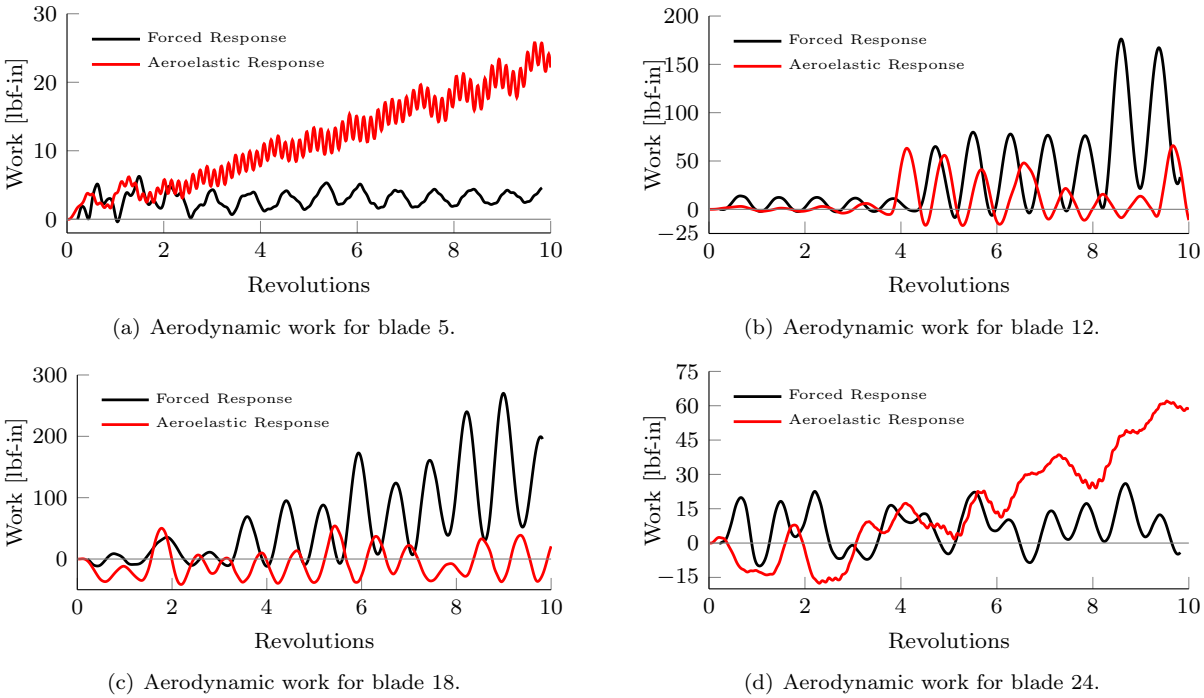

(a) Aerodynamic work for blade 5.

(b) Aerodynamic work for blade 12.

(c) Aerodynamic work for blade 18.

(d) Aerodynamic work for blade 24.

Figure 18. Comparison of aerodynamic work from the forced response and aeroelastic response calculations at the 100% throttle setting.

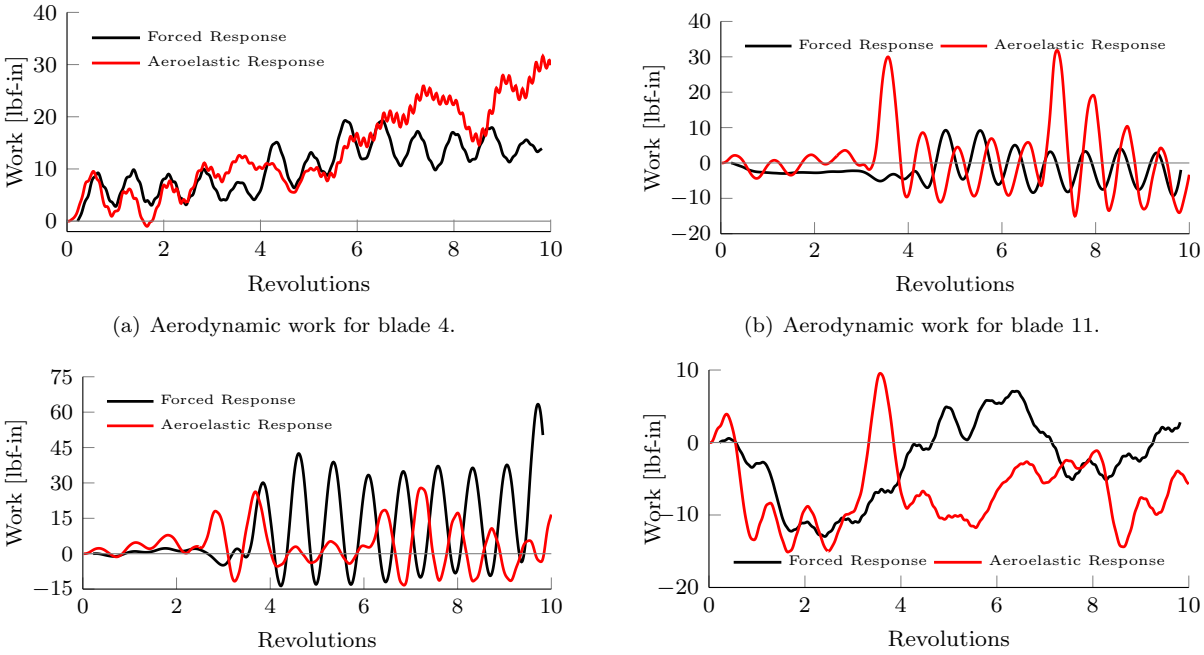

(a) Aerodynamic work for blade 4.

(b) Aerodynamic work for blade 11.

(c) Aerodynamic work for blade 14.

(d) Aerodynamic work for blade 24.

Figure 19. Comparison of aerodynamic work from the forced response and aeroelastic response calculations at the 75% throttle setting.

response increases at a similar rate to the forced response case, which may indicate a neutrally stable case where the blade is at the flutter margin. The aerodynamic work for blades 11, 16, and 22 is shown in Figs. 20(b)- 20(d). The aerodynamic work for these blades displays similarity between the aeroelastic and forced response calculations. This behavior suggests two possible situations: (a) neutral stability of the blades, or (b) the blade response is dominated by the unsteady aerodynamic loads induced by the bird damage. Comparison of the aerodynamic work for the remaining blades at the 60% throttle setting displays similar behavior and does not indicate potential aeroelastic instabilities.

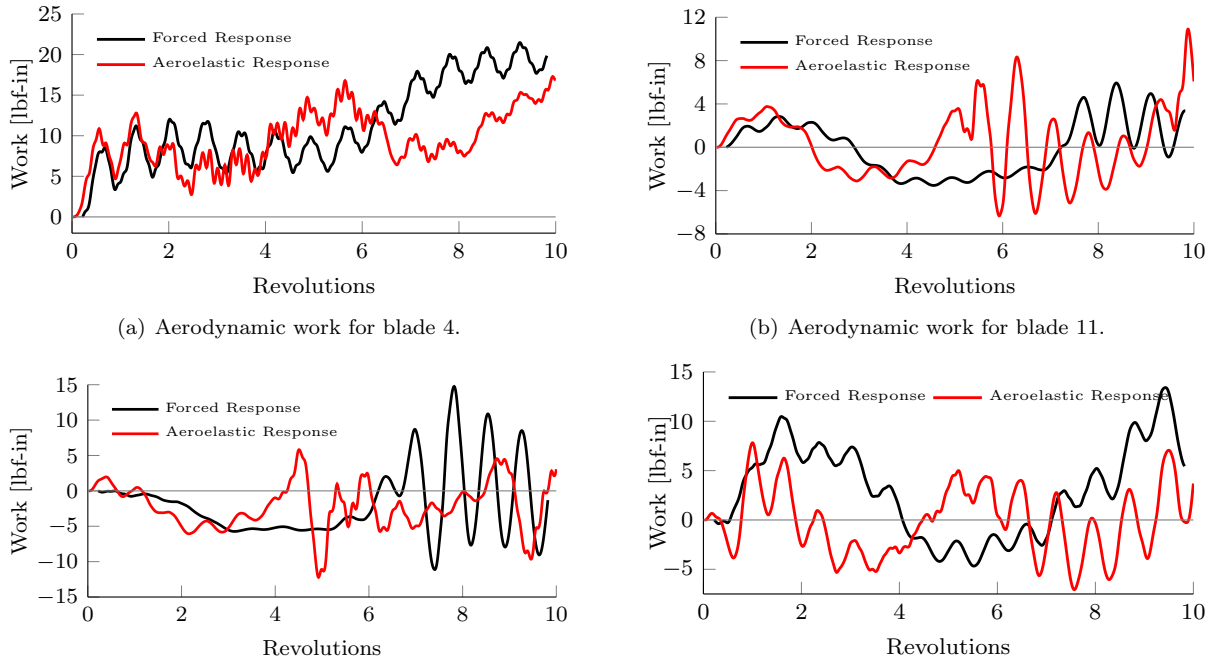

(a) Aerodynamic work for blade 4.

(b) Aerodynamic work for blade 11.

(c) Aerodynamic work for blade 14.

(d) Aerodynamic work for blade 24.

Figure 20. Comparison of aerodynamic work from the forced response and aeroelastic response calculations at the 60% throttle setting.

The results obtained indicate that for the cases considered, bird damage does not have a major effect on aeroelastic stability. The growth in structural response for the undamaged blades opposite the damaged sector appears to be dominated by the unsteady aerodynamic loads caused by the damaged blades. The damaged blades and those directly downstream of the damaged sector exhibit a possible aeroelastic instability in the second torsion mode for the 100% and 75% throttle settings. For the case of 100% throttle setting, the aeroelastic response indicates an instability dominated by the second torsion mode for blades 3, 5, and 24. By comparison at 75% throttle setting the aeroelastic response in the second torsion mode of blades 4 and 5 is indicative of an aeroelastic instability. The instability of these blades likely results from interaction between the blade motion and the unsteady wake shed from the upstream damaged blades. The tip displacements of these blades appear to reach a limit-cycle amplitude that is relatively small compared to those of the undamaged blades opposite the damaged sector.

VII. Concluding Remarks

Predicting the aeroelastic behavior of a bird-damaged fan represents a significant barrier in the development of improved-efficiency turbofan engines. In this study, a coupled CFD/CSD framework is employed to investigate numerically the structural response of a bird-damaged fan. A realistic fan configuration is considered that involves a sector of 5 damaged fan blades obtained through accurate numerical simulation of the bird strike event. Two computational frameworks are implemented to couple the CFD and CSD components: a one-way forced response framework, which neglects the feedback mechanism of the structural response on the unsteady aerodynamic loading, and a fully-coupled aeroelastic response framework that accounts for it. The forced response and aeroelastic response calculations are compared to identify the importance of

aeroelastic coupling in predicting the blade structural response. The effect of engine rotation is also explored by performing the calculations at the 100%, 75%, and 60% throttle settings, which correspond to FAA certification requirements for bird strike. Overall, the results emphasize several important characteristics of the damaged fan, which are summarized below:

1. The unsteady stall cell emanating from the damaged sector produces large unsteady aerodynamic loads that drive the blade response. At the 100% throttle setting, the stall cell detaches from the damaged sector and excites a majority of the blades. In contrast, the stall cell does not detach for the 75% and 60% throttle settings, and the undamaged blades upstream of the damaged sector are unaffected by the unsteady stall cell.

2. For all throttle settings considered, the undamaged blades opposite the damaged sector exhibit the largest response for both the forced response and aeroelastic response calculations.

3. Comparison of the aerodynamic work from the forced and aeroelastic response is useful for identification of the mechanism driving the response. It also allows one to assess the aeroelastic stability of the bird damaged fan.

4. The results indicate that the growth in blade response results primarily from the unsteady aerodynamic loads caused by the damaged fan blades rather than by an aeroelastic mechanism. This implies that aeroelastic effects are secondary to the forced response effects caused by the unsteady stall cell.

5. The aeroelastic responses of the damaged blades and those immediately counterclockwise from the damaged sector exhibit rapid growth that may be associated with aeroelastic instability of higher structural modes. The aeroelastic response at the 100% and 75% throttle settings show increased participation of the second torsion mode, particularly for the damaged blades and those directly downstream of the damaged sector. The 60% throttle setting calculations indicate an increased participation of the third bending mode for the damaged blades and those opposite the damaged sector.

While this study demonstrates the feasibility of performing aeroelastic response calculations of a bird-damaged fan, the computations require a significant investment in time that may prevent practical implementation for design purposes. The results show that the forced response approach, which is computationally less expensive, may be sufficient for predicting the blade response to a large extent. Thus the forced response may have a useful role in preliminary design of fans under bird strike conditions. These results were calculated assuming that structural damping is neglected. Including structural damping in the structural dynamic model may reduce or eliminate the aeroelastic instability noted.

References

[1]Teichmann, H. C. and Tadros, R. N., "Analytical and Experimental Simulation of Fan Blade Behavior and Damage Under Bird Impact," *Journal of Engineering for Gas Turbines and Power*, Vol. 113, No. 4, October 1991, pp. 582–594.

[2]Horsley, J., "The 'Rolls-Royce' Way of Validating Fan Integrity," *AIAA Paper No. 93-2602, AIAA/SAE/ASME/ASEE 29th Joint Propulsion Conference and Exhibit*, Monterey, CA, June 1993, pp. 1–22.

[3]Isomura, K. and Giles, M. B., "A Numerical Study of Flutter in a Transonic Fan," *Journal of Turbomachinery*, Vol. 120, No. 3, July 1998, pp. 500–507.

[4]LeMieux, J., *One Bird Strike and You're Out!: Solutions to Prevent Bird Strikes*, Trafford Publishing, Bloomington, Indiana, 2009.

[5]Eschenfelder, P., "Jet Engine Certification Standards," *Proceedings of the International Bird Strike Committee*, Amsterdam, April 2000, pp. 535–540.

[6]*Bird Ingestion*, 14 Code of Federal Regulations (CFR) §33.76 (2013).

[7]Bendiksen, O. O., "Aeroelastic Problems in Turbomachines," *Transactions of the ASME*, Vol. 113, October 1991, pp. 582–594.

[8]Bendiksen, O. O., Kielb, R. E., and Hall, K. C., "Structural Technology," *Encyclopedia of Aerospace Engineering*, Vol. 3, chap. Turbomachinery Aeroelasticity, John Wiley & Sons, 2010, pp. 1625–1639.

[9]Goyal, V. K., Huertas, C. A., Borrero, J. R., and Leutwiler, T. R., "Robust Bird-Strike Modeling Based on ALE Formulation Using LS-DYNA," *AIAA Paper No. 2006-1759, Proceedings of the 47th AIAA/ASME/ASCE/AHS/ASC Structures, Structural Dynamics, and Materials Conference*, Newport, RI, May 2006.

[10]Hirschbein, M. S., "Bird Impact Analysis Package for Turbine Engine Fan Blades," *AIAA Paper No. 1982-696, Proceedings of the 23rd AIAA/ASME/ASCE/AHS/ASC Structures, Structural Dynamics, and Materials Conference*, New Orleans, LA, May 1982.

[11]Mao, R., Meguid, S. A., and Ng, T. Y., "Finite Element Modeling of a Bird Striking an Engine Fan Blade," *Journal of Aircraft*, Vol. 44, No. 2, 2007, pp. 583–596.

[12]Mao, R., Meguid, S. A., and Ng, T. Y., "Transient Three Dimensional Finite Element Analysis of a Bird Striking a Fan Blade," *International Journal of Mechanics and Materials in Design*, Vol. 4, No. 1, 2008, pp. 79–96.

[13]Meguid, S. A., Mao, R., and Ng, T. Y., "FE Analysis of Geometry Effects of an Artificial Bird Striking an Aeroengine Fan Blade," *International Journal of Impact Engineering*, Vol. 35, No. 6, 2008, pp. 487–498.

[14]Nizampatnam, L. S. and Horn, W. J., "Investigation of Equation of State Models for Predicting Bird Impact Loads," *AIAA Paper No. 2008-682, Proceedings of the 46th AIAA Aerospace Sciences Meeting and Exhibit*, Reno, NV, January 2008.

[15]Shimamura, K., Shibue, T., and Grosch, D. J., "Numerical Simulation of Bird Strike Damage on Jet Engine Fan Blade," *Proceedings of the ASME/JSME Pressure Vessels and Piping Conference*, San Diego, CA, July 2004.

[16]Imregun, M. and Vahdati, M., "Aeroelastic Analysis of a Bird-Damaged Fan Assembly Using a Large Numerical Model," *The Aeronautical Journal*, Vol. 103, No. 1030, December 1999, pp. 569–578.

[17]Kim, M., Vahdati, M., and Imregun, M., "Aeroelastic Stability Analysis of a Bird-Damaged Aeroengine Assembly," *Journal of Aerospace Sciences and Technologies*, Vol. 5, No. 7, 2001, pp. 469–482.

[18]Aotsuka, M. and Tsuchiya, N., "Numerical Simulation of Transonic Fan Flutter with 3-D N-S CFD Code," *Proceedings of the ASME Turbo Expo 2008: Power for Land, Sea, and Air*, Berlin, Germany, June 2008.

[19]Marshall, J. G. and Imregun, M., "A Review of Aeroelasticity Methods with Emphasis on Turbomachinery Applications," *Journal of Fluids and Structures*, Vol. 10, No. 3, 1996, pp. 237–267.

[20]Bartels, R. E. and Sayma, A. I., "Computational Aeroelastic Modelling of Airframes and Turbomachinery: Progress and Challenges," *Philosophical Transactions of The Royal Society*, Vol. 365, No. 1859, October 2007, pp. 2469–2499.

[21]Verdon, J., "Review of Unsteady Aerodynamic Methods for Turbomachinery Aeroelastic and Aeroacoustic Applications," *AIAA Journal*, Vol. 31, No. 2, February 1993, pp. 235–250.

[22]Bendiksen, O. O., "Modern Developments in Computational Aeroelasticity," *Proceedings of the Institution of Mechanical Engineers, Part G: Journal of Aerospace Engineering*, Vol. 218, No. 3, 2004.

[23]Bohari, B. and Sayma, A., "CFD Analysis of Effects of Damage Due to Bird Strike on Fan Performance," *Proceedings of the ASME Turbo Expo 2010: Power for Land, Sea, and Air*, Glasgow, UK, June 2010.

[24]Muir, E. R. and Friedmann, P. P., "Aeroelastic Response of Bird-Damaged Fan Blades Using a Coupled CFD/CSD Framework," *AIAA Paper No. 2014-0334, Proceedings of the 55th AIAA/ASME/ASCE/AHS/ASC Structures, Structural Dynamics, and Materials Conference*, National Harbor, MD, January 2014.

[25]Muir, E. R. and Friedmann, P. P., "Unsteady Aerodynamic Loading on Bird-Damaged Fan Blades and Its Effect on Forced Response," *2013 International Forum on Aeroelasticity and Structural Dynamics*, Bristol, UK, June 2013.

[26]Muir, E. R. and Friedmann, P. P., "Unsteady Aerodynamic Analysis of a Bird-Damaged Turbofan," *AIAA Paper No. 2013-1773, Proceedings of the 54th AIAA/ASME/ASCE/AHS/ASC Structures, Structural Dynamics, and Materials Conference*, Boston, MA, April 2013.

[27]ANSYS Inc., *Ansys CFX-Solver Theory Guide - Version 14.5*, 2012.

[28]Muir, E. R., *Aeroelastic Behavior of Bird-Damaged Fan Blades Using a Coupled CFD/CSD Framework*, Ph.D. thesis, Dept. of Aerospace Engineering, University of Michigan, 2014.

[29]ANSYS Inc., *Mechanical APDL Theory Reference Guide - Version 14.5*, 2012.

[30]Hilber, H. M., Hughes, T. J. R., and Taylor, R. L., "Improved Numerical Dissipation for Time Integration Algorithm in Structural Dynamics," *Earthquake Engineering and Structural Dynamics*, Vol. 5, No. 3, July-September 1977, pp. 283–292.

[31]ANSYS Inc., *Mechanical APDL Coupled-Field Analysis Guide - Version 14.5*, 2012.